Supplimental Material: Phase transition kinetics revealed by *in situ* X-ray diffraction in laser-heated dynamic diamond anvil cells

Matthew Ricks,[1] Arianna E. Gleason,[2] Francesca Miozzi,[3] Hong Yang,[4] Stella Chariton,[5] Vitali B. Prakapenka,[5] Stanislav V. Sinogeikin,[6] Richard L. Sandberg,[1] Wendy L. Mao,[4] and Silvia Pandolfi[2, 7]

[1]*Department of Physics and Astronomy, Brigham Young University, Provo, Utah 84602, USA*
[2]*SLAC National Accelerator Laboratory, 2575 Sand Hill Rd., Menlo Park, CA, 94025, USA*
[3]*Earth and Planets Laboratory, Carnegie Institution for Science, Washington, DC 20015*
[4]*Department of Earth and Planetary Sciences, Stanford University,*
450 Jane Stanford Way, Building 320, Stanford, CA 94305
[5]*Center for Advanced Radiation Sources, The University of Chicago, Chicago, IL 60637*
[6]*DAC Tools, LLC, Naperville, Illinois 60565, USA*
[7]*Now at: Sorbonne Université, Muséum National d'Histoire Naturelle, UMR CNRS 7590,*
Institut de Minéralogie, de Physique des Matériaux et de Cosmochimie, IMPMC, 75005 Paris, France

I. DETAILED EXPERIMENTAL METHODS

Samples consisted of reagent-grade Fe powder with micrometer-sized grains, commercially available from Alfa Aesar. The samples were loaded in pre-indented stainless steel gaskets (30-40 μm-thick SS 304, initial thickness 250 μm). The diamonds had flat culets of 250 and 300 μm. The sample chamber (100 μm diameter) was drilled using an electrical discharge drilling system. Cold-pressed flakes of KCl were placed on either side of the Fe grains, providing thermal insulation from the diamond culets and acting as a pressure transmitting medium and a pressure calibrant with a well-known equation of state [1].

The sample assemblages were loaded in a mini-BX80 DAC developed by DAC Tools, which is a modified version of the mini-BX90 apparatus [2], and it was equipped with tungsten carbide seats. The mini-BX80 allows for pressure control either by screws or remotely, *e.g.*, using a membrane enclosure and an online remote control system [3]. To enable dynamic loading of the DAC using the membrane gas supply, our experimental setup included an intermediate buffer. The buffer allows us to pre-load the gas supply to a desired pressure, and it is located near the DAC. An electric solenoid valve allows release of the gas in the membrane on a short ($\sim$ms) timescale for high compression rate experiments (see FIG.1 of the main text). Analogous setups for fast compression and *in situ* characterization using synchrotron radiation have already been demonstrated at other facilities [4, 5].

Experiments were conducted at the 13-IDD beamline of the GSECARS sector of the Advanced Photon Source [6]. The highest compression rate that we achieved with this apparatus is >1 TPa/s, as shown in FIG.1. In the main text, we chose to analyze runs done at hundreds of GPa/s due to the stability of their temperature measurements.
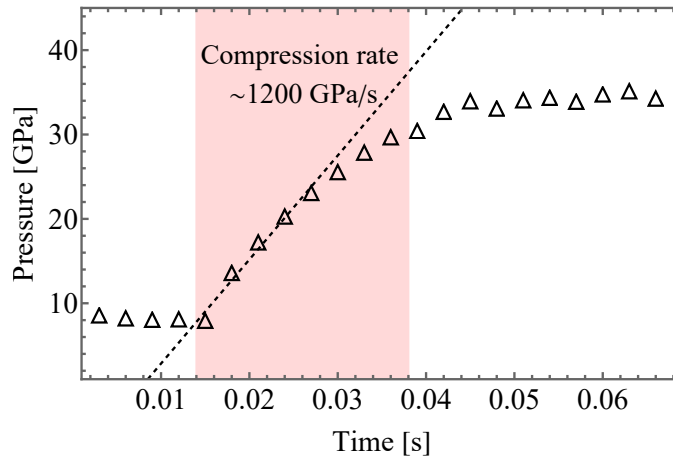

FIG. 1: The triangle symbols are the pressure values measured at 3 ms intervals. The dotted line is a linear fit of these data points during peak compression. These data are from the fastest run, compressing at a rate of 1200 GPa/s over 20 ms. After the loading cycle (highlighted in red), the sample continues to compress slowly over the next several seconds to its final pressure

X-ray diffraction data (XRD) was collected *in situ* at HP-HT using a monochromatic X-ray beam with energies of 42 and 37 keV and a Pilatus3 X 1M CdTe detector. X-ray wavelength was 0.3344 $\mathring{A}$. LaB_6 was used as reference to calibrate the detector distance and geometry. 1D integration from 2D detector images was done using the Fit2D and Dioptas software packages [7, 8]. Peak identification and fitting was conducted in the PDindexer software package [9]. When the intermediate buffer was engaged, the acquisition time was 2 ms/pattern; this ensured good temporal resolution for the characterization of the high-pressure phase transitions and an accurate determination of the transition onset. Changes in pressure were monitored using the known EOS of the B2 phase of KCl [1] and fitting of the KCl (110) reflection; this choice was dictated by the visibility of the KCl (110) reflection throughout the whole experiment and the lack of superposition with any Fe peaks. In all runs, the sample was initially compressed to 7 GPa, well past the phase boundary in KCl from the B1 to the B2 phase. This ensured more accurate pressure measurements, as the KCl does not undergo any structural transition over the explored pressure range.

Thanks to the short (less than 20 mm) working distance on both sides, the mini-BX80 cell equipped with membrane enclosure is compatible with the double-sided laser heating setup of the 13-IDD beamline [10]. Temperature was measured on both sides of the DAC with 300 ms temporal resolution by fitting a Planck equation to the thermal radiation spectrum [10]. The size of X-ray beam on the sample was $2\mu m$ (V) x $3.5\mu m$ (H) and the size of the flat-top laser-heating spot was 12 μm in diameter; the beams were coaxially aligned to spatially overlap. In runs at high temperature, the sample was first heated, and then pressure was increased using the buffer at HT.

II.   DATA TABLE

TABLE I: This is the data for each of the 1-D diffraction traces in FIG.3 of the main text. Also included is data from diffraction images taken several seconds after the phase transition onset. This data shows that the pressure cell continues to compress slowly for several seconds following peak compression and that the sample makes a complete transformation to the high pressure phase. Raw XRD for each of these will be made available upon reasonable request.

	Pressure (GPa)	Temperature (K)	Iron Phase	Compression rate GPa/s
Run 1	37	2000±250	γ	400
Run 1	40	2000±250	γ/ϵ	400
Run 1	41	2000±250	γ/ϵ	400
Run 1	46	2000±250	γ/ϵ	400
After Run 1	55	1900±115	ϵ	After compression
Run 2	18	1400±150	γ	530
Run 2	23	1400±150	γ/ϵ	530
Run 2	26	1400±150	γ/ϵ	530
Run 2	28	1400±150	γ/ϵ	530
After Run 2	28	1100±50	ϵ	After compression
Run 3	11.5	300	α	360
Run 3	12.5	300	α	360
Run 3	13.6	300	α/ϵ	360
Run 3	14.6	300	α/ϵ	360
After Run 3	20.2	300	ϵ	After compression
Run 4	7.6	300	α	2.5
Run 4	10.8	300	α/ϵ	2.5
Run 4	12.3	300	α/ϵ	2.5
Run 4	16.9	300	α/ϵ	2.5
After Run 4	28.6	300	ϵ	After compression

III.   DETAILED DATA ANAYSIS

A.   Calculating Error Bars

For the runs performed at high-temperature, the double-side laser heating and the controlled geometry of the assembly contribute to maintaining the axial gradient below 100 K [11]. Additional temperature uncertainty comes from the evolution of the sample emissivity with pressure, which is generally neglected. A final source of error comes from temperature fluctuations with time, particularly in the proximity of the phase transition. In Run 1, fluctuations remained below 150 K. In Run 2, fluctuations remained below 50 K. In summary, we assume the error on the temperature of the sample to be ±250 K in Run 1 and ±150 K in Run 2. Uncertainties in pressure were determined by fitting the thermal equation of the state of KCl by Tateno et al. with the upper and lower temperature values [1].
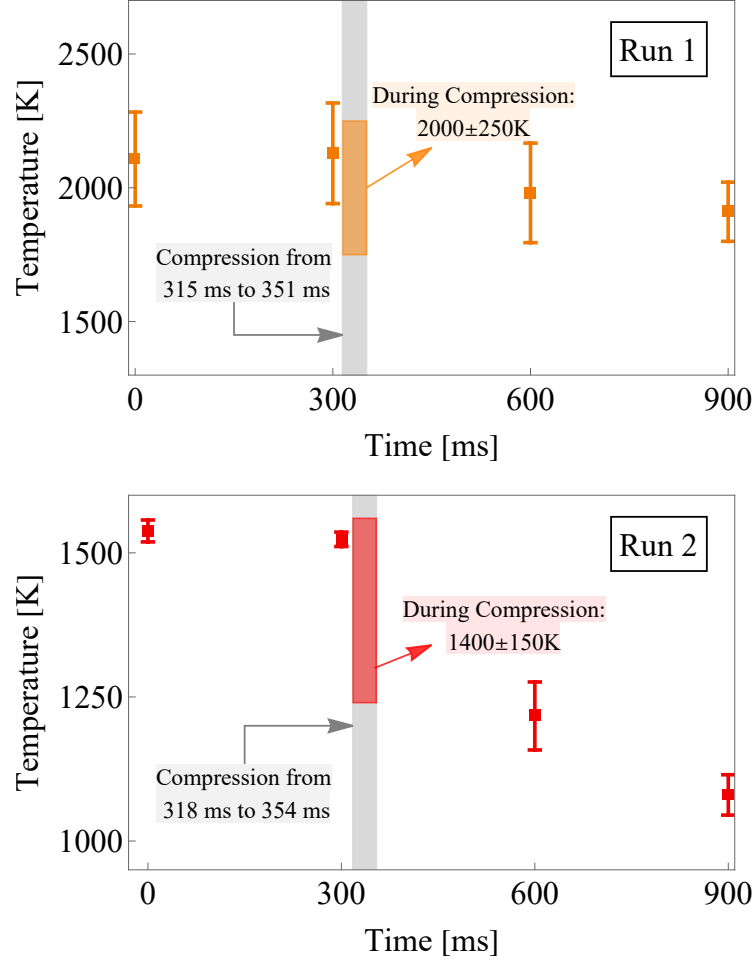
B.   Temperature measurements

FIG. 2: Temperature measurements were taken every 300 ms. These values are indicated with the orange and red squares. An explanation of how error bars were calculated is in Section III A. The sample was compressed after the second temperature measurement for the period indicated by the gray-shaded region

C.   Texture analysis

The quality of the XRD data collected *in situ* with ms aquisition time allows identification of the phases present at each investigated pressure. Additionally, longer-acquisition data was also collected before and after dynamic compression for more detailed texture analysis. Representative data from two distinct runs, done at an x-ray energy of 37 and 42 keV, is shown in FIG.3, in which 2D XRD data projected onto the 2θ-ϕ (azimuthal angle) space is overlaid with the 1D azimuthally integrated data to highlight the texture corresponding to each Fe phase. FIG.3 (a, d) shows the structure of the sample at 7 GPa and 300 K, prior to being heated or compressed dynamically; at these conditions, no phase transition is observed and the sample maintains the ambient Fe structure (α phase). FIG.3 (b, e) shows the sample transformation upon annealing at different temperatures; in particular, we notice that a higher temperature is required to ensure completion of the α-γ transformation at HT (1450 K rather than 1360 K). The reflections corresponding to the γ phase show a non-uniform intensity distribution over the Debye-Scherrer rings, along the ϕ direction. This indicates that this phase crystallizes in large grains that do not cover the whole range of orientations with respect to the X-ray beam. FIG.3 (c, f) shows the final state reached by the sample, after dynamic loading and quenching. In both cases, complete transition to the ϵ phase is observed; this phase appears to have wider XRD peaks with more uniform azimuthal intensity distribution compared with its precursor, which is indicative of a finely-grained powder. However, a strongly preferred orientation can be inferred by the low intensity of the ϵ-(002)
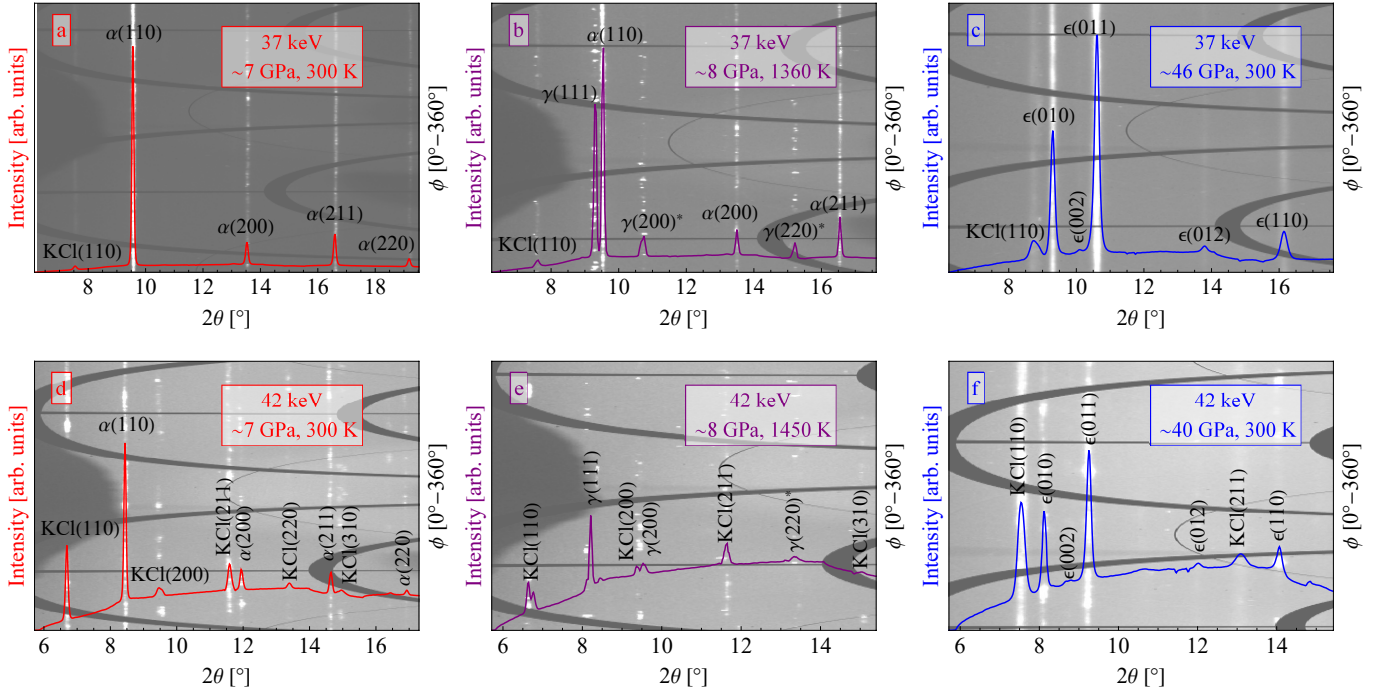
FIG. 3: 2D XRD data projected onto the 2θ-ϕ (azimuthal angle) space is overlaid with the 1D azimuthally integrated data. Data was acquired using 1s integration time. (a) and (d): structure and texture of the sample after static compression to 7 GPa at 300 K. (b) and (e): structural and textural changes occurring after heating at HP up to 1360 K and 1450 K, respectively. (c) and (f): samples' structure after dynamic loading and quench down to 300 K; in both cases, the final Fe structure corresponds to the ϵ phase.

reflection; this is expected, as the $\epsilon[002]$ direction is the most compressible one in this phase. It is also interesting to note that, in the case of a pure γ precursor (FIG.3(c,f)), the ϵ appears more textured than in the case of a mixed α and γ precursor (FIG.3(b,c)). Therefore, it is plausible that on the millisecond compression timescale, the ϵ texture perseveres an imprint of the precursor's texture.

D. Degree of quasi-hydrostaticity

In previous HP studies, deviations of the transition pressure from the equilibrium phase diagram have been attributed to highly non-hydrostatic pressure states [12, 13]. To investigate the degree of quasi-hydrostaticity in the sample chamber and whether it could have influenced the observed phase transition onsets, we have analyzed the axial ratio of the ϵ crystalline structure. Indeed, the hexagonal unit cell is described by two lattice parameters, a in the hexagonal plane, and c in the stacking direction; the c axis is the most compressible and tends to align with the compression axis in DAC experiment In high pressure studies, despite not providing a direct measurement of hydrosticity, deviations of the c/a ratio from the reference value are routinely analyzed and interpreted as signature of largely non-hydrostatic states, $i.e.$, presence of large uniaxial stress components. FIG.4 shows the c/a ratio of the ϵ phase calculated from our experimental data and compared with previous results from the literature [14, 15]. Konôpková et $al.$ measured the c/a ratio both in quasi-hydrostatic and non-hydrostatic conditions, $i.e.$, with and without the use of a pressure transmitting medium, giving a reliable reference for the c/a values measured in either condition. Our results are in good agreement with the degree of quasi-hydrostaticity of previous DAC studies performed at lower compression rates, that reported no noticeable shift in the phase boundaries[14, 15]; thus, the onset shifts here observed cannot be ascribed to a lower degree of quasi-hydrostaticity compared to previous studies.
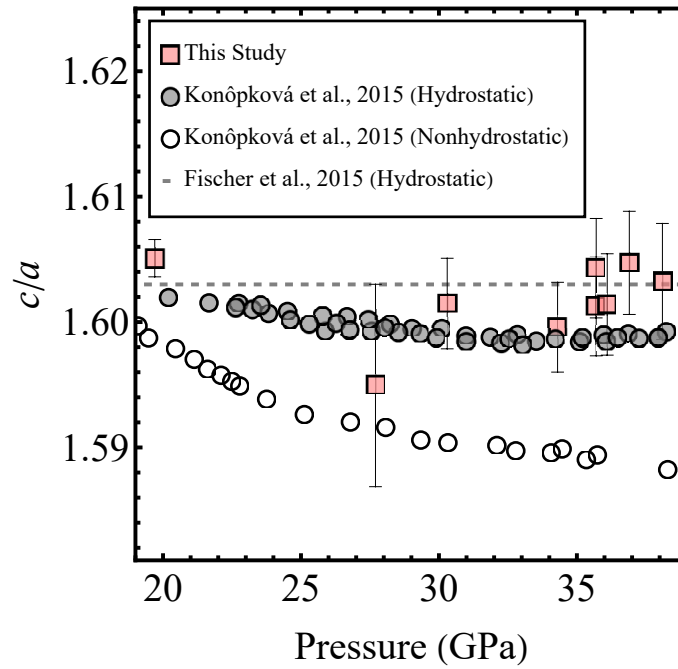
FIG. 4: Hydrostaticity analysis, by measuring the c/a ratio of the hcp cell parameters as a function of pressure. Our data (pink symbols) are compared with previous experiments in hydrostatic conditions by Fischer et $al.$ [15] and with results from Konôpková et $al.$[14]. In the latter study, results for both hydrostatic (solid symbols) and non-hydrostatic (empty symbols) were reported.

[1] S. Tateno, T. Komabayashi, K. Hirose, N. Hirao, and Y. Ohishi, Static compression of B2 KCl to 230 GPa and its P-V-T equation of state, American Mineralogist **104**, 718 (2019).

[2] I. Kantor, V. Prakapenka, A. Kantor, P. Dera, A. Kurnosov, S. Sinogeikin, N. Dubrovinskaia, and L. Dubrovinsky, Bx90: A new diamond anvil cell design for x-ray diffraction and optical measurements, Review of Scientific Instruments **83**, 125102 (2012).

[3] S. V. Sinogeikin, J. S. Smith, E. Rod, C. Lin, C. Kenney-Benson, and G. Shen, Online remote control systems for static and dynamic compression and decompression using diamond anvil cells, Review of Scientific Instruments **86**, 072209 (2015).

[4] N. Velisavljevic, S. Sinogeikin, R. Saavedra, R. S. Chellappa, A. Rothkirch, D. M. Dattelbaum, Z. Konopkova, H.-P. Liermann, M. Bishop, G. M. Tsoi, and Y. K. Vohra, Time-resolved x-ray diffraction and electrical resistance measurements of structural phase transitions in zirconium, Journal of Physics: Conference Series **500**, 032020 (2014).

[5] B. Haberl, M. Guthrie, B. D. Malone, J. S. Smith, S. V. Sinogeikin, M. L. Cohen, J. S. Williams, G. Shen, and J. E. Bradby, Controlled formation of metastable germanium polymorphs, Phys. Rev. B **89**, 144111 (2014).

[6] G. Shen, V. B. Prakapenka, P. J. Eng, M. L. Rivers, and S. R. Sutton, Facilities for high-pressure research with the diamond anvil cell at GSECARS, Journal of Synchrotron Radiation **12**, 642 (2005).

[7] A. P. Hammersley, S. O. Svensson, M. Hanfland, A. N. Fitch, and D. Häusermann, Two-dimensional detector software: From real detector to idealised image or two-theta scan, High Pressure Research **14**, 235 (1996).

[8] C. Prescher and V. B. Prakapenka, Dioptas: a program for reduction of two-dimensional x-ray diffraction data and data exploration, High Pressure Research **35**, 223 (2015), https://doi.org/10.1080/08957959.2015.1059835.

[9] Y. Seto, D. Nishio-Hamane, T. Nagai, and N. Sata, Development of a software suite on x-ray diffraction experiments, The Review of High Pressure Science and Technology **20**, 269 (2010).

[10] V. B. Prakapenka, A. Kubo, A. Kuznetsov, A. Laskin, O. Shkurikhin, P. Dera, M. L. Rivers, and S. R. Sutton, Advanced flat top laser heating system for high pressure research at gsecars: application to the melting behavior of germanium, High Pressure Research **28**, 225 (2008).

[11] A. J. Campbell, C. T. Seagle, D. L. Heinz, G. Shen, and V. B. Prakapenka, Partial melting in the iron-sulfur system at high pressure: A synchrotron x-ray diffraction study, Physics of the Earth and Planetary Interiors **162**, 119 (2007).

[12] R. D. Taylor, M. P. Pasternak, and R. Jeanloz, Hysteresis in the high pressure transformation of bcc- to hcp-iron, Journal of Applied Physics **69**, 6126 (1991), https://doi.org/10.1063/1.348779.

[13] N. A. Zarkevich and D. D. Johnson, Coexistence pressure for a martensitic transformation from theory and experiment: Revisiting the bcc-hcp transition of iron under pressure, Phys. Rev. B **91**, 174104 (2015).

[14] Z. Konôpková, A. Rothkirch, A. K. Singh, S. Speziale, and H.-P. Liermann, In situ x-ray diffraction of fast compressed iron: Analysis of strains and stress under non-hydrostatic pressure, Phys. Rev. B **91**, 144101 (2015).

[15] R. A. Fischer and A. J. Campbell, The axial ratio of hcp fe and fe-ni-si alloys to the conditions of earth's inner core, American Mineralogist **100**, 2718 (2015).